



ELSEVIER

Contents lists available at ScienceDirect

Journal of Sound and Vibration

journal homepage: www.elsevier.com/locate/jsvi

Nonlinear dynamic characteristics of a quasi-zero stiffness vibration isolator with cam–roller–spring mechanisms



Jiaxi Zhou^a, Xinlong Wang^a, Daolin Xu^{a,*}, Steve Bishop^b

^a State Key Laboratory of Advanced Design and Manufacturing for Vehicle Body, College of Mechanical and Vehicle Engineering, Hunan University, Changsha 410082, PR China

^b Department of Mathematics, University College London, Gower Street, London WC1E 6BT, UK

ARTICLE INFO

Article history:

Received 17 August 2014

Received in revised form

22 January 2015

Accepted 4 February 2015

Handling Editor: D.J. Wagg

Available online 16 March 2015

ABSTRACT

The property of quasi-zero stiffness (QZS) of vibration isolation system (VIS) could be realized by using the conceptual design of cam–roller–spring mechanisms (CRSMs). We develop this idea into a physical prototype and study its vibration isolation performance. A piecewise nonlinear dynamic model is formulated in the consideration of possible disengagement between the cam and roller. The analytical solution of the amplitude–frequency relationship is derived by using the averaging method and further verified by numerical simulations. The effects of excitation force and system damping on the force transmissibility are investigated. A particular behavior of this type of QZS isolator, very differ from existing ones, is that the peak transmissibility and starting frequency of isolation never overshoots those of the linear counterpart no matter how large the excitation amplitude is. The prototype is tested and the experimental results show that the QZS isolator outperforms the linear counterpart.

© 2015 Elsevier Ltd. All rights reserved.

1. Introduction

For a linear vibration isolation system (VIS), the performance of vibration isolation can be only effective when the excitation frequency is larger than $\sqrt{2}$ times the natural frequency of the system. This limitation confines a linear VIS to attenuate vibration in low frequency band. To extend attenuation ability to low frequency domain, the decrease of the stiffness of the VIS could improve the vibration isolation performance but it could cause undesirable large deflection. Ideally we would like a vibration isolation system with the characteristic of high-static and low-dynamic stiffness (HSLDS). Recently nonlinear VIS systems with quasi-zero stiffness [1–9] have been developed which integrate negative and positive elements of stiffness to achieve the property of high-static and low-dynamic stiffness. This type of nonlinear VIS can provide sufficiently large static stiffness to reduce static deflection, meanwhile offer very small dynamic stiffness about the static equilibrium position.

The early study of QZS systems started in the field of ground vibration testing of large aircraft. Woodard and Housner [10] applied a zero-spring-rate suspension system to the ground vibration tests of large flexible space structures, which requires a very soft suspension system to simulate the flight modes. The zero-spring-rate mechanism was realized by using two horizontal pre-compressed beams to produce negative stiffness in the vertical direction. This allows the stiffness of the

* Correspondence to: College of Mechanical and Vehicle Engineering, Hunan University, Changsha 410082, PR China.

E-mail addresses: jxizhou@hnu.edu.cn (J. Zhou), dlxu@hnu.edu.cn (D. Xu).

suspension system to be substantially diminished, becoming zero at the horizontal position of pre-compressed beams. In fact, zero-spring-rate suspension systems are a type of QZS systems. At the same time, QZS systems were developed to protect equipments from vibrations, especially for low-frequency vibrations. Alabuzhev et al. [1] comprehensively reviewed the design methodology and theory of vibration protecting systems with QZS characteristic. Platus [11] proposed a compact 6-dof passive VIS with negative-stiffness-mechanisms to counteract the stiffness of a spring suspension, leading to zero stiffness at the static equilibrium position and thereby producing ultra-low resonant frequency of the VIS.

A QZS system can be implemented by many different mechanisms [2] with the same principle, i.e. adding negative-stiffness-mechanisms to positive stiffness systems. Carrella et al. [3,4] considered a simple model by combining vertical springs (i.e. positive element) in parallel with oblique springs (i.e. negative element), and investigated the static and dynamic characteristics of VIS with QZS. Their results indicated that the QZS isolator outperforms the corresponding linear one under excitations but only if the amplitudes of the forcing excitation is small. In our previous work [8] a five-spring model [3] was developed and experimentally tested. We found that there is no jumping phenomenon for the transmissibility curves due to the damping caused by the friction of hinges, and confirmed the superiority of QZS isolator, especially for low-frequency excitations. Xu et al. [9] proposed a QZS isolator consisting of horizontal magnetic springs and vertical coil spring, and the analytical and experimental studies led to the same conclusions as those in Ref. [8]. Carrella and Friswell [12] proposed a HSLDS isolator that could be implemented by connecting a linear spring in parallel with the transverse flexure of a composite bistable plate. Furthermore, Shaw et al. [13] built an apparatus of this type of HSLDS isolator, and measured the dynamic response under base excitations, showing a greater isolation region and a lower peak response than the equivalent linear system. Liu et al. [14] developed a QZS mechanism by Euler buckled beams, while Zhou and Liu [15] devised a passive/semi-active electromagnetic vibration isolator for a tunable HSLDS. In report [15] the mass (a permanent magnet) was supported by a steel beam, whose transverse stiffness was counteracted by the negative stiffness of the magnetic springs. A low and near constant dynamic stiffness could be realized by adjusting the gap distance and electromagnet current, leading to an interesting feature for low-frequency vibration isolation. Sun et al. [16] proposed a simple linear time-delayed active control strategy to improve the system robustness in stability at the equilibrium position and system transmissibility performance. Tang and Brennan [17] studied the shock isolation characteristics of a QZS isolator subject to base excitation, and found that the QZS isolator has the best shock performance under shock with small amplitude. Ahn [18] reported a uniform symmetric nonlinear model in the form of odd power polynomials to represent various types of QZS vibration isolators, which enhanced the feasibility of analytical analysis.

For more detailed information about QZS systems for vibration isolation the interesting readers can refer to a comprehensive review report by Ibrahim [2] which includes various mechanisms and engineering design. Of specific note, the conceptual design of QZS isolator with cam–roller–spring mechanism first appeared in monograph [1]. Although this model was repeatedly reviewed later in documents [2,18], the detailed analysis and experimental test of the cam–roller–spring QZS system have never been investigated. Attracted by its compact design, we were motivated to study the dynamic characteristics of the cam–roller–spring QZS system.

In this paper, a new design of QZS isolator is proposed along with cam–roller–spring mechanism. Considering possible disengagement between the cam and the roller when the vibration amplitude is relatively large, a piecewise nonlinear dynamic model is developed to analyze its static and dynamic characteristics. The fundamental harmonic solutions are found by the averaging method [19]. The solutions are used to derive the amplitude–frequency relationship, and to describe the transmissibility of vibration isolation, and to study the effects of excitation amplitude, damping ratio and geometric parameters on the force transmissibility. To ensure the actual performance of the cam–roller–spring QZS system, a prototype is manufactured and experimental tests are conducted.

The rest of the paper is organized as follows. Section 2 elaborates the details of the model development of the cam–roller–spring mechanism. In Section 3, the piecewise nonlinear dynamic model and theoretical analysis are presented, including solutions of fundamental harmonic responses, the amplitude–frequency relationship, and the parameters region for contact and disengagement. Section 4 presents the dynamic behaviors and vibration isolation performance. In Section 5 the experimental tests are conducted to verify the isolation performance in terms of force transmissibility of the QZS VIS together with the comparison of the linear counterpart. Finally, Section 6 draws some conclusions of the present work.

2. The model of cam–roller–spring mechanism

A physical model of QZS isolator with cam–roller–spring mechanism is developed, according to the design concept initially proposed by Alabuzhev et al. [1], as shown in Fig. 1. The cam–roller–spring mechanism (CRSM) is indicated in Fig. 1a by a dash-line box which consists of a semi-circular cam, a roller and a horizontal spring. The loading support carries a mass M , and can only move in the vertical direction. The isolator is initially in the static equilibrium position, as shown in the Fig. 1, such that the centers of the semicircular cam and the roller lie on the same horizontal line, and the vertical and horizontal springs are compressed by deflection $\Delta x = Mg/k_v$ and δ , respectively, where Mg is the payload and k_v is the stiffness of vertical spring. In order to tune up the QZS property, the compression δ can be adjusted by the horizontal adjuster (7), and two vertical adjusters (6) screwed on the sliding rod (11) can ensure the alignment of the centers of the semi-circular cam and the center of the roller in horizontal when the supporting mass M changes. For example, when the mass increases by ΔM , the relative distance between the two vertical adjusters should be increased by $\Delta d_v = \Delta Mg/k_v$. When the loading support oscillates vertically about the equilibrium position, the center of semicircular cam deviates from

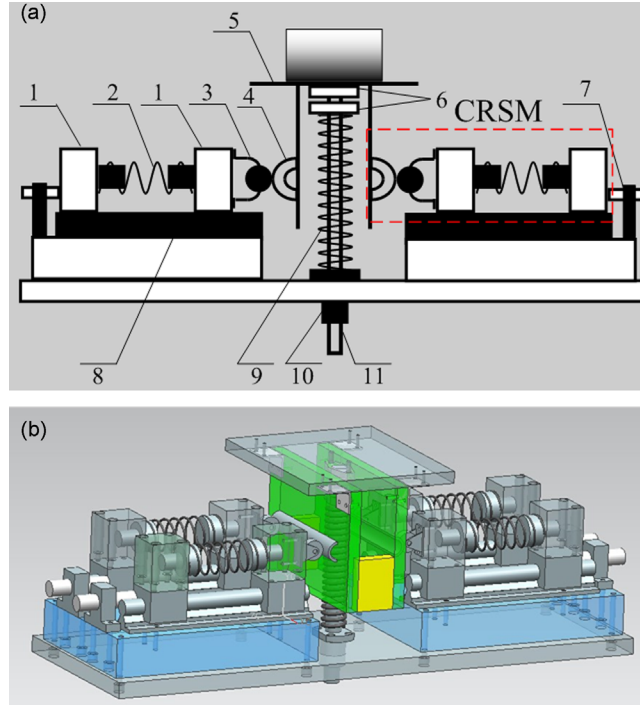


Fig. 1. A QZS vibration isolator with cam-roller-spring mechanism: (a) schematic diagram; (b) physical model; 1–slider, 2–horizontal spring with stiffness k_h , 3–roller with radius r_1 , 4–semi-circular cam with radius r_2 , 5–loading support, 6–vertical adjuster, 7–horizontal adjuster, 8–sliding rail, 9–vertical spring with stiffness k_v , 10–linear bearing with flat flange, and 11–sliding rod.

this position, and the CRSM acts as a negative stiffness element, which can reduce the system's stiffness in the vertical direction. When the negative stiffness at the equilibrium position is equal to the stiffness of the vertical spring, the stiffness of the isolator in vertical direction will become zero, hence the so-called zero-stiffness condition.

To understand the cam-roller-spring mechanism, we study the relationship between force and displacement, and further extend the discussion to the stiffness property. With the payload, the equilibrium position is shown in Fig. 2a. When applying a force f , it causes a vertical displacement x from the static equilibrium position, as shown in Fig. 2b. When $|x| < x_d = \sqrt{r_2(2r_1+r_2)}$, the roller maintains in contact with the cam, as depicted in Fig. 2c. The critical position for the disengagement between the cam and roller is depicted in Fig. 2d. However, when $|x| > x_d$, the roller will detach from the cam and move along the vertical wall of the support, as shown in Fig. 2e. Therefore, the relationship between the applied force and the displacement can be represented in a piecewise manner. It is noted that the magnitude of the restoring force of the system is equal to the applied force, but in opposite direction.

When the roller touches on the cam, the relationship between the applied force and the displacement can be given by

$$f(x) = Mg - f_v - 2f_h \tan \theta \quad (1)$$

where vertical spring force is $f_v = k_v(\Delta x - x)$, horizontal spring force $f_h = k_h[\delta - (r_1 + r_2)(1 - \cos \theta)]$, and $\tan \theta = x / \sqrt{(r_1 + r_2)^2 - x^2}$. Recall that the vertical spring is compressed by a deflection Δx to support the payload at the static equilibrium position. Hence, the relationship between the applied force f and the displacement x is

$$f(x) = k_v x - 2k_h x \left[1 + \frac{\delta - (r_1 + r_2)}{\sqrt{(r_1 + r_2)^2 - x^2}} \right] \quad (2)$$

When the displacement x exceeds the critical value x_d , the roller will detach from the cam. Once this happens, the horizontal spring no longer contributes towards the vertical force. Therefore, the mass is supported just by the vertical spring, and the applied force f can be written as

$$f(x) = k_v x \quad (3)$$

Combining Eqs. (2) and (3), the applied force can be written by

$$f(x) = \begin{cases} k_v x - 2k_h x \left[1 + \frac{\delta - (r_1 + r_2)}{\sqrt{(r_1 + r_2)^2 - x^2}} \right] & |x| < x_d \\ k_v x & |x| \geq x_d \end{cases} \quad (4)$$

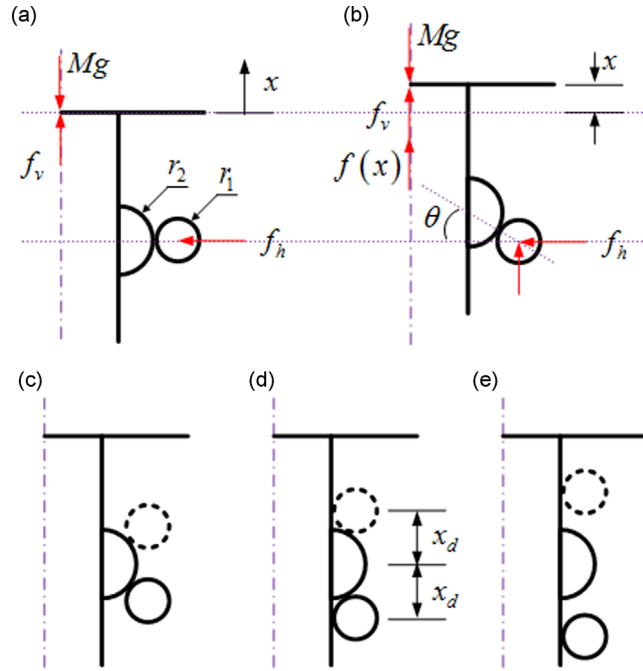


Fig. 2. Schematic diagram of static analysis of the support and the roller: (a) at equilibrium position; (b) deviation from equilibrium position by a displacement x , and three typical positions between the cam and roller: (c) in contact; (d) critical position of contact; and (e) disengagement.

Let $\bar{x} = x/(r_1 + r_2)$ and $\bar{f} = f/k_v(r_1 + r_2)$, the above equations can be rewritten in non-dimensional form

$$\bar{f}(x) = \begin{cases} \bar{x} - 2\alpha\bar{x} \left[1 + \frac{\bar{\delta}-1}{\sqrt{1-\bar{x}^2}} \right] & |\bar{x}| < \bar{x}_d \\ \bar{x} & |\bar{x}| \geq \bar{x}_d \end{cases} \quad (5)$$

where $\bar{\delta} = \delta/(r_1 + r_2)$ and $\alpha = k_h/k_v$, and

$$\bar{x}_d = \frac{\sqrt{2\eta+1}}{\eta+1} \quad (6)$$

where $\eta = r_1/r_2$.

Considering small oscillations about the equilibrium position, i.e., $|\bar{x}| < \bar{x}_d$, the non-dimensional stiffness of the system can be obtained by differentiating the first expression of Eq. (5) with respect to the non-dimensional displacement.

$$\bar{K} = 1 - 2\alpha \left[1 + \frac{\bar{\delta}-1}{(1-\bar{x}^2)^{3/2}} \right] \quad (7)$$

The non-dimensional force–displacement and stiffness characteristics are shown in Figs. 3 and 4, respectively, for different compressions $\bar{\delta}$ of the horizontal spring at the equilibrium position. When the compressed deflection is large, such as $\bar{\delta} = 0.8$, the static force–displacement behavior is dominated by horizontal springs, leading to negative stiffness in the region near the static equilibrium position. Conversely, a small compression, such as $\bar{\delta} = 0.3$, results in positive stiffness. As expected, there is a unique relationship between the parameters α and $\bar{\delta}$, resulting in zero stiffness characteristics at the static equilibrium position, which can be established by setting $\bar{K}(\bar{x} = 0) = 0$. Thus it yields the QZS condition

$$\bar{\delta}_{QZS} = \frac{1}{2\alpha} \quad (8)$$

The variations of the applied force and the stiffness plotted against the displacement are depicted in Figs. 3 and 4, respectively, where the solid lines indicate the QZS characteristics about equilibrium.

By substituting Eq. (8) into the first expression of Eq. (5), the force–displacement relationship of the QZS system can be given by

$$\bar{f}_{QZS}(\bar{x}) = \bar{x} \left[1 - \frac{1}{\bar{\delta}_{QZS}} \left(1 + \frac{\bar{\delta}_{QZS}-1}{\sqrt{1-\bar{x}^2}} \right) \right] \quad (9)$$

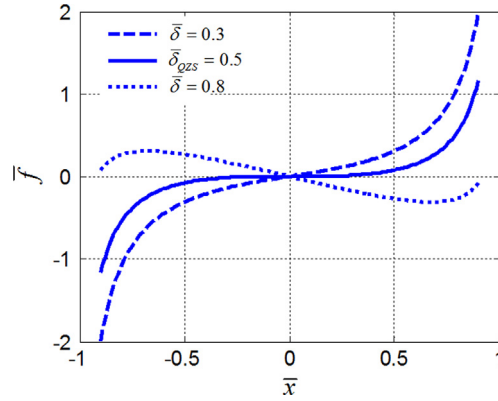


Fig. 3. Force–displacement curves with $\alpha = 1$ and $\eta = 0.5$

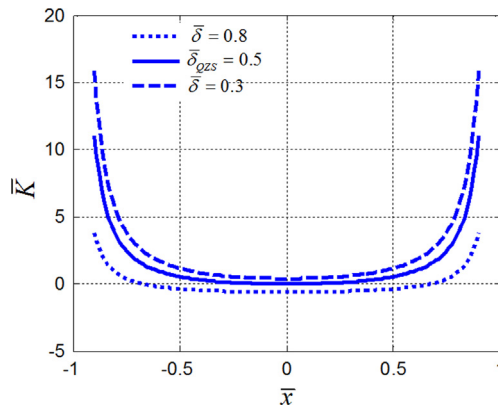


Fig. 4. Stiffness–displacement curves with $\alpha = 1$ and $\eta = 0.5$

and the stiffness of the QZS system can be given by

$$\bar{K}_{QZS} = 1 - \frac{1}{\bar{\delta}_{QZS}} \left[1 + \frac{\bar{\delta}_{QZS} - 1}{(1 - \bar{x}^2)^{3/2}} \right] \quad (10)$$

The non-dimensional stiffness is depicted as a function of non-dimensional displacement in Fig. 5. When $\bar{\delta}_{QZS} < 1$, the system stiffness is positive, and the increase rate of the stiffness decreases about equilibrium as $\bar{\delta}_{QZS}$ increases. When $\bar{\delta}_{QZS} > 1$, the system stiffness appears undesirable negative. For the special value of $\bar{\delta}_{QZS} = 1$, the system stiffness is zero throughout the whole displacement range, namely the system will lose the holding capability of the payload, which is also unwanted in design. Therefore, the design space for $\bar{\delta}_{QZS}$ is $(0, 1)$. Considering real applications, one can assign an optimal value of $\bar{\delta}_{QZS}$ in terms of transmissibility based on the actual vibration amplitude.

In order to simplify the subsequent dynamic analysis, as carried out by Carrella et al. [3], the relationship between the force and displacement of the QZS system depicted in Fig. 6 will be approximated by a cubic function using a truncated Taylor series expansion about the equilibrium. By expanding Eq. (9) about $\bar{x} = 0$, the force can be approximately rewritten as

$$\bar{f}_{QZS}(\bar{x}) = \frac{1 - \bar{\delta}_{QZS}}{2\bar{\delta}_{QZS}} \bar{x}^3 \quad (11)$$

and the approximate stiffness can be given by

$$\bar{K}_{QZS}(\bar{x}) = \frac{3(1 - \bar{\delta}_{QZS})}{2\bar{\delta}_{QZS}} \bar{x}^2 \quad (12)$$

Including the disengagement, the complete expression of the restoring force of the QZS isolator is given by

$$\bar{f}_{QZS}(\bar{x}) = \begin{cases} \left[1 - \frac{1}{\bar{\delta}_{QZS}} \left(1 + \frac{\bar{\delta}_{QZS} - 1}{\sqrt{1 - \bar{x}^2}} \right) \right] \bar{x} & |\bar{x}| < \bar{x}_d \\ \bar{x} & |\bar{x}| \geq \bar{x}_d \end{cases} \quad (13)$$

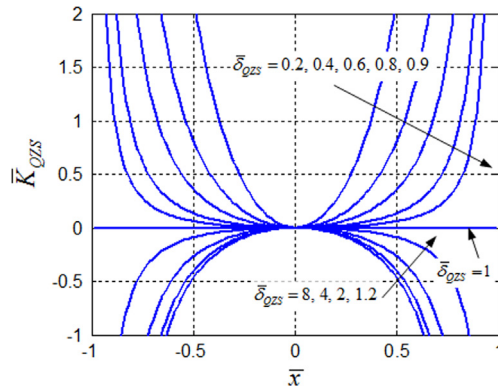


Fig. 5. Non-dimensional stiffness of the QZS system when $|\bar{x}| < \bar{x}_d$ and $\eta = 0.5$.

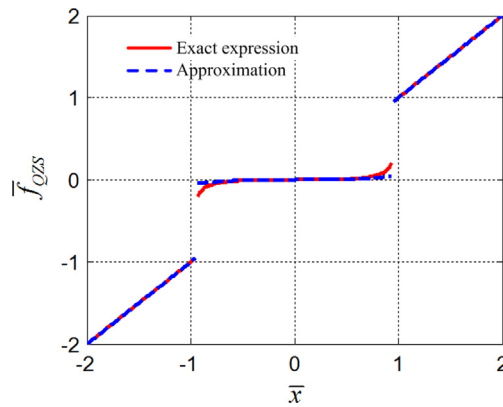


Fig. 6. Exact force–displacement relationship compared with the approximation when $\bar{\delta}_{QZS} = 0.9$, and $\eta = 0.5$.

and the complete expression of the stiffness of the QZS isolator can be written by

$$\bar{K}_{QZS} = \begin{cases} 1 - \frac{1}{\bar{\delta}_{QZS}} \left[1 + \frac{\bar{\delta}_{QZS} - 1}{(1 - \bar{x}^2)^{3/2}} \right] & |\bar{x}| < \bar{x}_d \\ 1 & |\bar{x}| \geq \bar{x}_d \end{cases} \quad (14)$$

To obtain the analytical solution of the system dynamics, the exact expression for the restoring force in Eq. (13) will be replaced by the approximate form in Eq. (11). As a result, the approximate expression of the restoring force can be given by

$$\bar{f}_{QZS}^a(\bar{x}) = \begin{cases} \gamma \bar{x}^3 & |\bar{x}| < \bar{x}_d \\ \bar{x} & |\bar{x}| \geq \bar{x}_d \end{cases} \quad (15)$$

where $\gamma = (1 - \bar{\delta}_{QZS}) / (2\bar{\delta}_{QZS})$.

The exact force–displacement relationship of the system and its approximation are depicted in Fig. 6. The restoring force undergoes a discontinuous jump at the critical position $|\bar{x}| = \bar{x}_d$ approximately 1. Apart from the regions near \bar{x}_d the approximation closely matches the force–displacement curve.

3. Amplitude–frequency relationship and critical condition for contact

A linear viscous damper is added in parallel with the vertical spring so that the equation of motion for the vibration isolation system under harmonic excitation is given by

$$M\ddot{x} + c\dot{x} + f(x) = F_0 \cos \omega t \quad (16)$$

where F_0 is the excitation amplitude, c is the damping coefficient, and $f(x)$ is the restoring force defined by Eq. (4). For the QZS system, the equation of motion can be written in non-dimensional form as

$$\bar{x}'' + 2\zeta\bar{x}' + \bar{f}_{QZS}(\bar{x}) = \bar{F}_0 \cos \Omega\bar{t} \quad (17)$$

where

$$\bar{x} = \frac{x}{r_1 + r_2}, \quad \bar{F}_0 = \frac{F_0}{k_v(r_1 + r_2)}, \quad \bar{t} = \sqrt{\frac{k_v}{M}}t, \quad \Omega = \frac{\omega}{\sqrt{k_v/M}}, \quad \zeta = \frac{c}{2\sqrt{Mk_v}}$$

and where the prime (') denotes differentiation with respect to \bar{t} , and $\bar{f}_{QZS}(\bar{x})$ is defined by Eq. (13). As mentioned previously, the restoring force can be simplified to be a cubic function. The dynamic equation, therefore, is approximately given by

$$\bar{x}'' + 2\zeta\bar{x}' + \bar{f}_{QZS}^a(\bar{x}) = \bar{F}_0 \cos \Omega\bar{t} \tag{18}$$

where $\bar{f}_{QZS}^a(\bar{x})$ is defined by Eq. (15).

Due to the piecewise nonlinearity, the fundamental solution of the dynamic equation will be obtained by the averaging method [19]. The dynamic equation (18) can be rearranged as

$$\bar{x}'' + \Omega_0^2\bar{x} = \bar{F}_0 \cos \Omega\bar{t} - 2\zeta\bar{x}' - h(\bar{x}) \tag{19}$$

where $\Omega_0 = 1$ and

$$h(\bar{x}) = \begin{cases} -\bar{x} + \gamma\bar{x}^3 & |\bar{x}| < \bar{x}_d \\ 0 & |\bar{x}| \geq \bar{x}_d \end{cases} \tag{20}$$

By introducing $\Omega_0^2 = \Omega^2 - \varepsilon\sigma$ and multiplying the right of Eq. (19) by ε , the dynamic equation can be further rewritten as

$$\bar{x}'' + \Omega^2\bar{x} = \varepsilon g(\bar{x}, \bar{x}', \bar{t}) + \varepsilon\sigma\bar{x} \tag{21}$$

where ε is a small parameter, and σ is a detuning parameter, and

$$g(\bar{x}, \bar{x}', \bar{t}) = \bar{F}_0 \cos \Omega\bar{t} - 2\zeta\bar{x}' - h(\bar{x}) \tag{22}$$

When $\varepsilon = 0$, the solution of Eq. (21) is given by

$$\bar{x} = A \cos(\Omega\bar{t} - \theta), \quad \bar{x}' = -\Omega A \sin(\Omega\bar{t} - \theta) \tag{23}$$

where A and θ are constants. When $\varepsilon \neq 0$, the solution of Eq. (21) can still be represented by Eq. (23), but A and θ are functions with respect to \bar{t} rather than constants. By introducing $\psi(\bar{t}) = \Omega\bar{t} - \theta$ and substituting ψ into Eq. (23), and then differentiating Eq. (23) with respect to \bar{t} , we obtain

$$\begin{cases} \bar{x}' = A' \cos \psi - A(\Omega - \theta') \sin \psi \\ \bar{x}'' = -\Omega[A' \sin \psi + A(\Omega - \theta') \cos \psi] \end{cases} \tag{24}$$

By substituting the second equation of Eq. (23) and Eq. (21) into Eq. (24), and solving the algebra equation with respect to A' and θ' , we can get

$$\begin{cases} A' = -\frac{\varepsilon}{2\pi\Omega} [g(\bar{x}, \bar{x}', \bar{t}) + \sigma\bar{x}] \sin \psi \\ \theta' = \frac{\varepsilon}{2\pi A} [g(\bar{x}, \bar{x}', \bar{t}) + \sigma\bar{x}] \cos \psi \end{cases} \tag{25}$$

Eq. (25) suggests that the variations of A' and θ' against \bar{t} have the same magnitude as the small parameter ε , which are much slower than the change of ψ against \bar{t} . Their averages are assumed to be constant over a period of 2π . Therefore,

$$\begin{cases} A' = -\frac{\varepsilon}{2\pi\Omega} \int_{-\pi}^{\pi} [g(\bar{x}, \bar{x}', \bar{t}) + \sigma\bar{x}] \sin \psi \, d\psi = -\frac{\varepsilon}{2\Omega} (2\zeta A \Omega - \bar{F}_0 \sin \theta) \\ \theta' = \frac{\varepsilon}{2\pi A} \int_{-\pi}^{\pi} [g(\bar{x}, \bar{x}', \bar{t}) + \sigma\bar{x}] \cos \psi \, d\psi = \frac{\varepsilon}{2\Omega A} (\bar{F}_0 \cos \theta + \sigma A + \frac{H}{\pi}) \end{cases} \tag{26}$$

where

$$H = \begin{cases} \frac{\pi}{4} (4A - 3\gamma A^3) & A < \bar{x}_d \\ \left(\gamma\bar{x}_d^3 + \frac{3\gamma A^2 - 4\bar{x}_d}{2} \right) \frac{\sqrt{A^2 - \bar{x}_d^2}}{A} + \frac{4A - 3\gamma A^3}{4} \left[\pi - 2\arccos\left(\frac{\bar{x}_d}{A}\right) \right] & A \geq \bar{x}_d \end{cases} \tag{27}$$

Steady periodic motions occur when $A' = 0$ and $\theta' = 0$, which corresponds to the solutions of

$$\begin{cases} \bar{F}_0 \sin \theta = 2\zeta A \Omega \\ \bar{F}_0 \cos \theta = -\sigma A - \frac{H}{\pi} \end{cases} \tag{28}$$

Substituting $\sigma = (\Omega^2 - \Omega_0^2)/\varepsilon$ into Eq. (28), and then letting $\varepsilon = 1$, and further squaring and adding these equations lead to the so-called amplitude–frequency (AF) equation

$$(2\zeta A \Omega)^2 + \left[(\Omega^2 - 1)A + \frac{H}{\pi} \right]^2 - (\bar{F}_0)^2 = 0 \tag{29}$$

It is interesting to find the critical condition of contact between the cam and roller according to the amplitude–frequency relationship (29). From Eqs. (27) and (29), the amplitude–frequency (A-F) equation for the case of contact ($A < \bar{x}_d$) can be

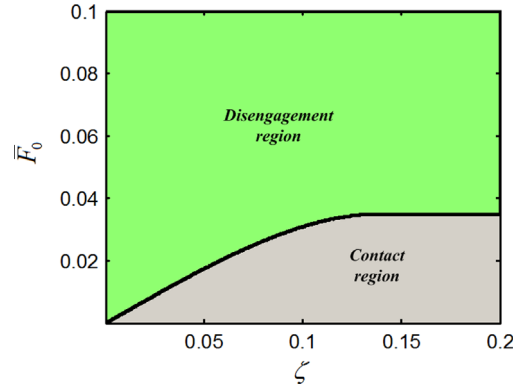


Fig. 7. Parameters region (ζ, \bar{F}_0) for contact and disengagement between the cam and roller.

given by

$$(2\zeta A\Omega)^2 + \left[\Omega^2 A + \frac{3}{4}\gamma A^3 \right]^2 - (\bar{F}_0)^2 = 0 \quad (30)$$

Solving the above quadratic equation for Ω^2 gives

$$\Omega_{1,2} = \sqrt{\frac{3}{4}\gamma A^2 - 2\zeta^2} \pm \frac{1}{A} \sqrt{4\zeta^4 A^2 - 3\zeta^2 \gamma A^4 + \bar{F}_0^2} \quad (31)$$

which implies two branches of solutions for the amplitude–frequency curve. When $\Omega_1 = \Omega_2$, the amplitude A reaches its maximum, namely a resonance peak, and it yields

$$4\zeta^4 A^2 - 3\zeta^2 \gamma A^4 + \bar{F}_0^2 = 0 \quad (32)$$

subjected to the constrain $A \geq 2\zeta \sqrt{(2/3\gamma)}$. Solving the above equation gives the resonance peak of amplitude

$$A_{\max,1} = \sqrt{\frac{2\zeta^3 + \sqrt{4\zeta^6 + 3\gamma\bar{F}_0^2}}{3\zeta\gamma}} \quad (33)$$

and $A_{\max,1}$ should be simultaneously satisfy $A_{\max,1} \geq 2\zeta \sqrt{(2/3\gamma)}$.

In the condition of $A_{\max,1} < 2\zeta \sqrt{(2/3\gamma)}$, where the system damping is significantly large, Eq. (30) has a unique solution, and the resonance branch will disappear, so that the amplitude monotonously decreases as the excitation frequency Ω increases. Therefore, the maximum amplitude happens at the zero excitation frequency, i.e.

$$\sqrt{\frac{3}{4}\gamma A^2 - 2\zeta^2} \pm \frac{1}{A} \sqrt{4\zeta^4 A^2 - 3\zeta^2 \gamma A^4 + \bar{F}_0^2} = 0 \quad (34)$$

and hence the maximum amplitude $A_{\max,2}$ can be obtained by solving the above equation, yields

$$A_{\max,2} = \sqrt[3]{\frac{4\bar{F}_0}{3\gamma}} \quad (35)$$

Obviously, when $A_{\max,1} \geq 2\zeta \sqrt{(2/3\gamma)}$, the maximum displacement amplitude $A_{\max,1}$ is related to the excitation amplitude \bar{F}_0 and the damping ζ ; however when $A_{\max,1} < 2\zeta \sqrt{(2/3\gamma)}$, $A_{\max,2}$ is dependent only on the excitation amplitude \bar{F}_0 . The parameters region for the contact can be approximately determined by the inequalities of both $A_{\max,1} < \bar{x}_d$ and $A_{\max,2} < \bar{x}_d$, and the result is shown in Fig. 7. For the parameters selected from the gray area, so-called *contact region*, the cam always maintains in contact with the roller. The borderline (solid line) indicates the critical parameters for the occurrence of disengagement where either the resonance peak reaches to $A_{\max,1} = \bar{x}_d$ in the case of small damping or the maximum amplitude hits $A_{\max,2} = \bar{x}_d$ at zero frequency for large damping.

4. Dynamic behaviors of the QZS vibration isolation system

In this section, we shall illustrate a variety of dynamic behaviors of the QZS system, including the feature of vibration amplitude against the excitation frequency, parameter effects on the dynamic behaviors, complex dynamics and the transmissibility of vibration isolation.

4.1. Verification of analytical solutions

The analytical solutions derived in Section 3 will be employed for the dynamic analysis of the QZS system. It is necessary to verify the correctness of theoretical solutions by means of numerical experiments. For an example of the parameter setting of $\bar{\delta}_{QZS} = 0.9$, $\eta = 0.5$, $\bar{F}_0 = 0.0833$ and $\zeta = 0.01$, the amplitude–frequency curves are plot in Fig. 8 based on the analytical and numerical methods. In the analytical results (by solving Eq. (29)), the stable solution are denoted by solid lines and unstable solutions are denoted by dashed lines. For the numerical solutions, the symbols ‘o’ and ‘+’ indicate the numerical solutions of Eqs. (17) and (18), respectively, by using the Runge–Kutta scheme with the fixed time step size set to one percent of excitation period. The numerical solutions are obtained by using both forward and backward frequency sweeps.

It can be seen that there is a good agreement between analytical solutions and their numerical counterparts. The amplitude–frequency curve on the lower branch, where $A < \bar{x}_d$, indicates the responses of the QZS system in the case of contact, while the amplitude–frequency curve on the upper branch, where $A \geq \bar{x}_d$, illustrates the responses of the QZS system in the case of disengagement. The coincidence between analytical and numerical results suggests that the cubic approximation for the restoring force (15) is adequate.

It is interesting to note that there is a unique frequency range, in which Eq. (29) has two solutions, one is stable but the other is unstable, as shown in Fig. 8 for frequencies between 0.35376 and 0.43276. It is can be verified by solving Eq. (26) with respect to A and θ from any initial conditions. We find that the response of A always converges toward the same value (a stable solution) from any initial conditions for the excitation frequency in this frequency range.

4.2. Parameter effects on amplitude–frequency response

The displacement A–F responses, which are numerical solutions of Eq. (29), are considerably influenced by the excitation amplitude, as can be seen from Fig. 9. When the excitation amplitude is ten percent of the weight of the mass, i.e. $\bar{F}_0 = 0.0167$, the displacement amplitudes on the resonance branch are close to \bar{x}_d , and the maximum amplitude is 1.072. Moreover, the maximum amplitude rises as the excitation amplitude increases. An excitation with a relatively large amplitude, such as 25 percent of the weight of the mass, i.e. $\bar{F}_0 = 0.0417$, will induce resonance at $\Omega = 1$, leading to a large

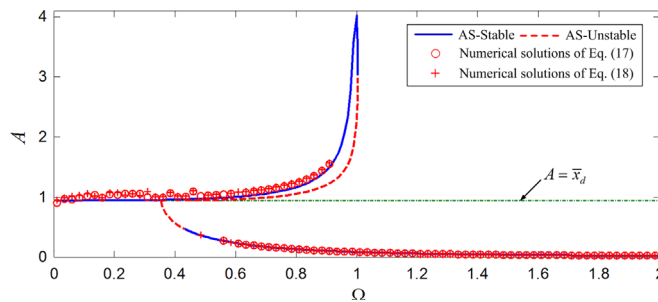


Fig. 8. Displacement A–F responses of the QZS system. Solid lines and dash line denote stable and unstable analytical solutions (AS) of Eq. (18), respectively, and o and + denote numerical solutions of Eqs. (17) and (18), respectively, when $\bar{\delta}_{QZS} = 0.9$, $\eta = 0.5$, $\bar{F}_0 = 0.0833$, and $\zeta = 0.01$.

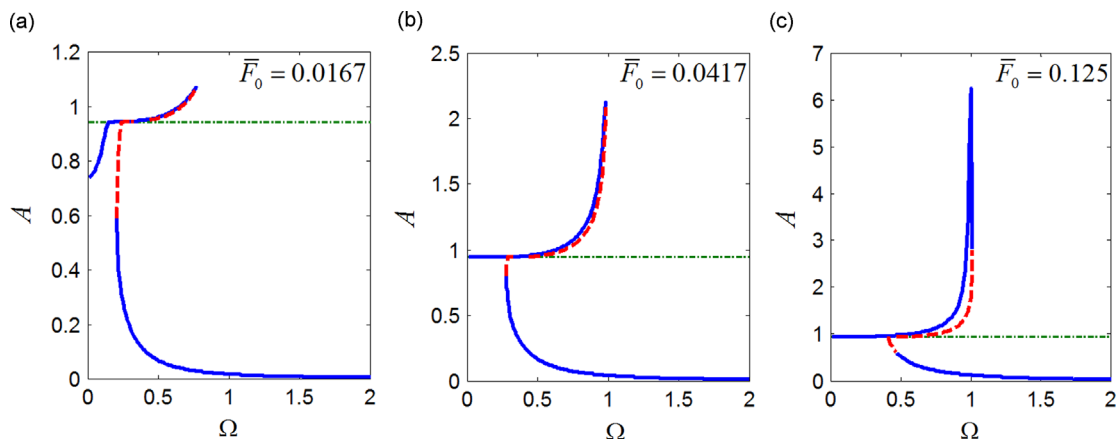


Fig. 9. Influence of excitation amplitude on A–F responses, when $\bar{\delta}_{QZS} = 0.9$, $\eta = 0.5$, and $\zeta = 0.01$.

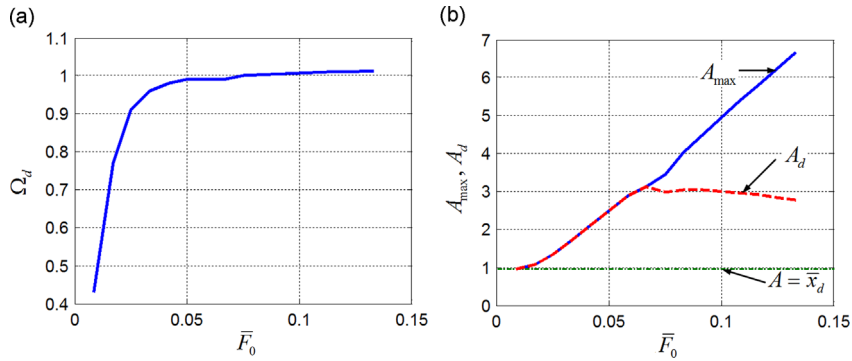


Fig. 10. Jump-down frequency (a), and maximum amplitude and amplitude at jump-down frequency (b) as functions of excitation amplitude, when $\bar{\delta}_{QZS} = 0.9$, $\eta = 0.5$, and $\zeta = 0.01$.

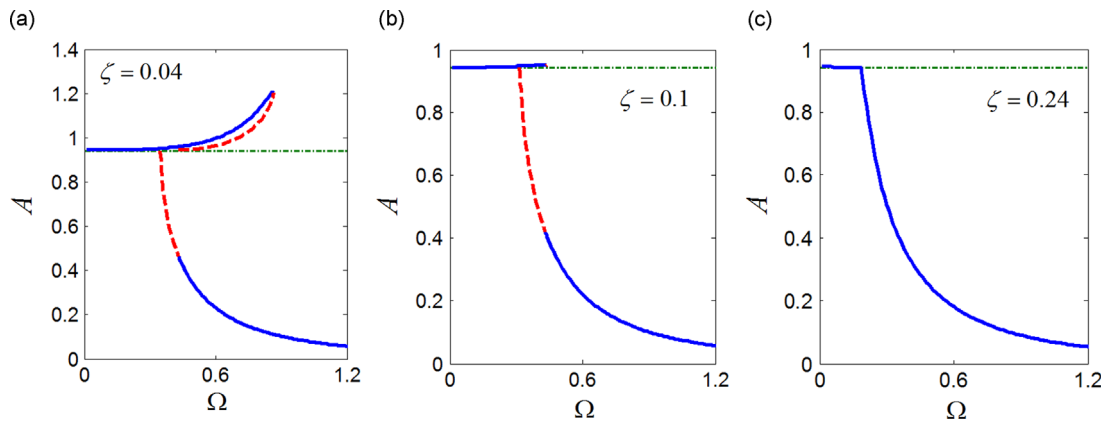


Fig. 11. Influence of damping on A–F responses, when $\bar{\delta}_{QZS} = 0.9$, $\eta = 0.5$, $\bar{F}_0 = 0.0833$.

displacement amplitude. It can also be seen that the displacement amplitude is always close to \bar{x}_d for the excitation frequency below the jump-up frequency.

The jump-down frequency Ω_d , the maximum amplitude A_{\max} , and the amplitude at jump-down frequency A_d as a function of excitation amplitude are shown in Fig. 10, respectively. It is observed that the jump-down frequency sharply increases as the excitation amplitude increases up to 0.05, but it increases slightly when the jump-down frequency is close to 1, i.e. the natural frequency of the linear system. As seen from Fig. 10b, when the resonance at $\Omega = 1$ occurs, the jump-down frequency slightly exceeds 1, and the maximum amplitude is much larger than the amplitude at jump-down frequency. Furthermore, the maximum amplitude almost varies linearly against \bar{F}_0 when the resonance at $\Omega = 1$ occurs, as the behavior appears in the linear system.

The resonance is extremely sensitive to damping. Concretely, the resonance branch of the A–F curve dramatically diminishes as the damping ratio increases, and is eliminated even by relatively light damping, which is illustrated in Fig. 11.

Fig. 12 shows variations of the jump-down frequency Ω_d and the maximum displacement amplitude A_{\max} as well as the amplitude at jump-down frequency A_d against the damping ratio. It can be seen that increasing damping reduces Ω_d , A_{\max} and A_d . When the damping is very light, the reduction of A_{\max} and A_d is obviously sharp. However, the variations of A_{\max} and A_d are very small and they are close to \bar{x}_d when the damping is relatively heavy. Therefore, a reasonable damping can effectively reduce the jump-down frequency and suppress the displacement amplitude, which is beneficial to the design of nonlinear vibration isolation systems. It should be noted that because of difficulty to find the analytical solutions of Eq. (29), the explicit expressions of Ω_d , A_{\max} and A_d with respect to \bar{F}_0 and ζ are not given in this paper. Therefore, Eq. (29) is solved numerically using Matlab Function *fsolve*, and conclusions in this section are drawn based on the graphical observation.

The influence of the ratio of rollers' radius to that of semicircular cams, i.e. η , on the A–F response is plotted in Fig. 13. The expression of \bar{x}_d given by Eq. (6) indicates that the increasing η reduces \bar{x}_d and makes the roller much more readily disengage from the cam, which is also illustrated by Fig. 13. It can be seen that large η results in occurrence of resonance at $\Omega = 1$, which suggests that resonance appears more easily for larger η . However, the maximum amplitude diminishes slightly as η increases.

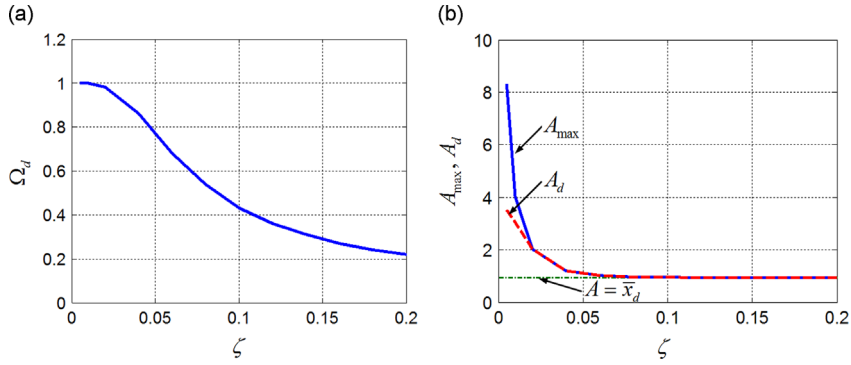


Fig. 12. Jump-down frequency (a), and maximum amplitude and amplitude at jump-down frequency (b) as functions of damping factor, when $\bar{\delta}_{QZS} = 0.9$, $\eta = 0.5$, $\bar{F}_0 = 0.0833$.

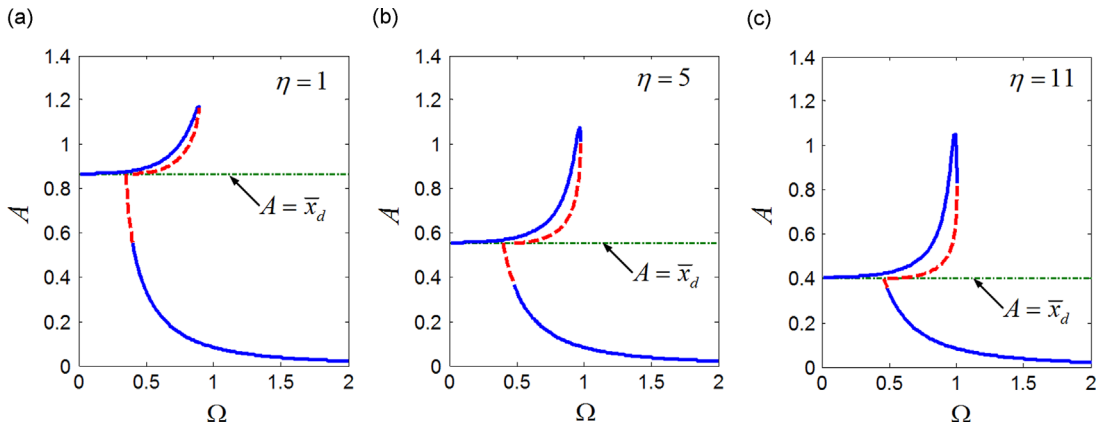


Fig. 13. Influence of η on A-F responses, when $\bar{\delta}_{QZS} = 0.9$, $\bar{F}_0 = 0.0833$, and $\zeta = 0.01$.

4.3. Complex dynamics of the QZS vibration isolation system

The bifurcation diagram with respect to the excitation amplitude is shown in Fig. 14, for the excitation frequency of $\Omega = 0.2$. The data of maximum amplitudes in this diagram are sampled using Poincaré sections. Note that a sampling rule for the Poincaré sections is to choose $t_n = nT$, when the period of the harmonic excitation is T . It is seen from Fig. 14a that there exists a chaotic parameter range of excitation amplitude, in which the system experiences complex dynamic motions. As seen from Fig. 14d, the trajectory of orbits fills up a section of the phase space, and Poincaré sections consist of a collection of unorganized points. Those observations suggest that the motion of the system with light damping is chaotic [20]. The route to chaos by period doubling is also observed.

In the jumping range, the displacement amplitude is determined by the initial conditions. The phase portraits and the corresponding Poincaré sections of resonant and non-resonant responses are depicted in Fig. 15, respectively. Obviously, the resonant amplitude is much larger than that of the non-resonant one. Moreover, the trajectory of orbits of the resonant response is so unique that it is completely different from that of the non-resonant one, due to the fact that the resonant response experiences two stages having entirely different stiffness. It is observed that the roller passes through the range, where the roller keeps touch with the cam, almost at a constant velocity.

4.4. Force transmissibility

By assuming that the response is dominated by the fundamental harmonic response, the force transmitting to the base can be given by

$$\bar{f}_t(\bar{t}) = \begin{cases} -2\zeta\Omega A \sin \psi + \gamma A^3 \cos^3 \psi \approx -2\zeta\Omega A \sin \psi + \frac{3}{4}\gamma A^3 \cos \psi & A < \bar{x}_d \\ -2\zeta\Omega A \sin \psi + A \cos \psi & A \geq \bar{x}_d \end{cases} \quad (36)$$

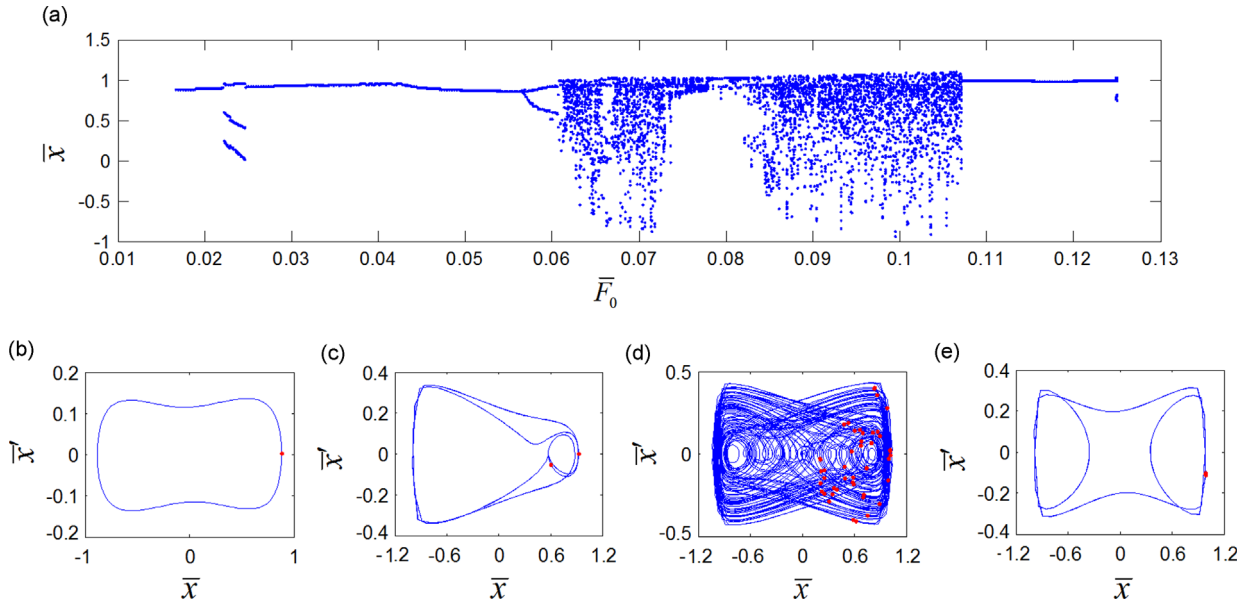


Fig. 14. Bifurcation with respect to excitation amplitude (a) and phase portraits and corresponding Poincaré sections of responses: (b) $\bar{F}_0 = 0.0167$, (c) $\bar{F}_0 = 0.06$, (d) $\bar{F}_0 = 0.07$, (e) $\bar{F}_0 = 0.12$, when $\bar{\delta}_{QZS} = 0.9$, $\eta = 0.5$, $\Omega = 0.2$, and $\zeta = 0.01$.

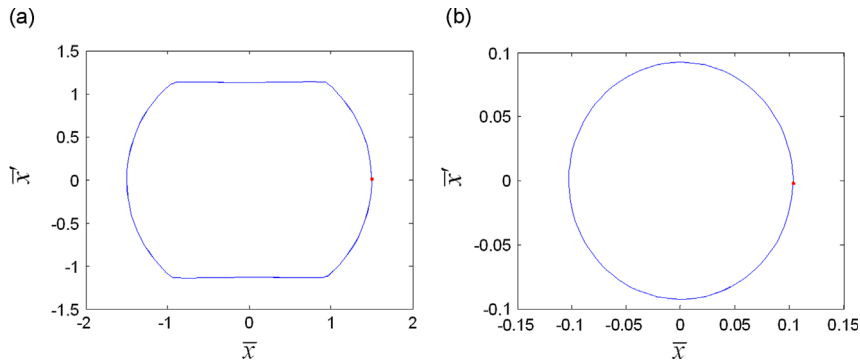


Fig. 15. Phase portraits and corresponding Poincaré sections of responses: (a) resonance and (b) non-resonance, when $\bar{\delta}_{QZS} = 0.9$, $\eta = 0.5$, $\Omega = 0.9$, $\zeta = 0.01$, and $\bar{F}_0 = 0.0833$.

Therefore, the force transmissibility, defined as the ratio of the amplitude of the force transmitted to the base to that of excitation force, can be written in the form of decibel

$$T = \begin{cases} 20\log_{10}\left(\sqrt{\frac{9\gamma^2 A^6/16 + (2\zeta\Omega)^2 A^2}{\bar{F}_0^2}}\right) & A < \bar{x}_d \\ 20\log_{10}\left(\sqrt{\frac{A^2 + (2\zeta\Omega)^2 A^2}{\bar{F}_0^2}}\right) & A \geq \bar{x}_d \end{cases} \quad (37)$$

It should be noted that both the expressions of the transmitted force and the force transmissibility are discontinuous, due to the discontinuousness of the restoring force at $|\bar{x}| = \bar{x}_d$, as mentioned in Section 2.

As shown in Fig. 14, the system under excitations with different amplitudes will experience complicatedly dynamical behaviors, such as sub/sup-harmonic motion, quasi-periodic motion and chaotic motion. Generally, for those types of motions, the force transmissibility cannot be explicitly evaluated by Eq. (37); however, it can be represented in the statistical form, which is defined as the ratio of root mean square (RMS) of response to that of the excitation [21,22], i.e.

$$T' = 20\log_{10}\left(\frac{\text{RMS}[\bar{f}_t(\bar{t}_i)]}{\text{RMS}[\bar{f}(\bar{t}_i)]}\right) \quad (38)$$

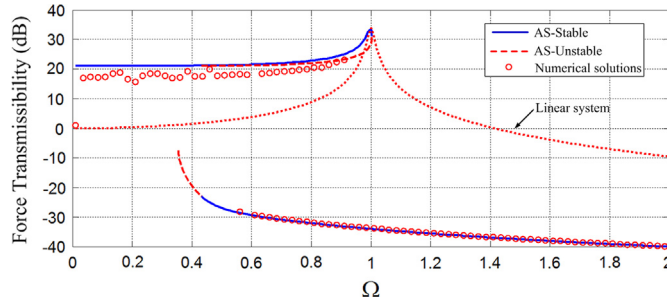


Fig. 16. Force transmissibility. Solid lines and dash line denote stable and unstable analytical results, respectively, and \circ denotes numerical results, when $\bar{\delta}_{QZS} = 0.9$, $\eta = 0.5$, $\zeta = 0.01$, $\bar{F}_0 = 0.0833$.

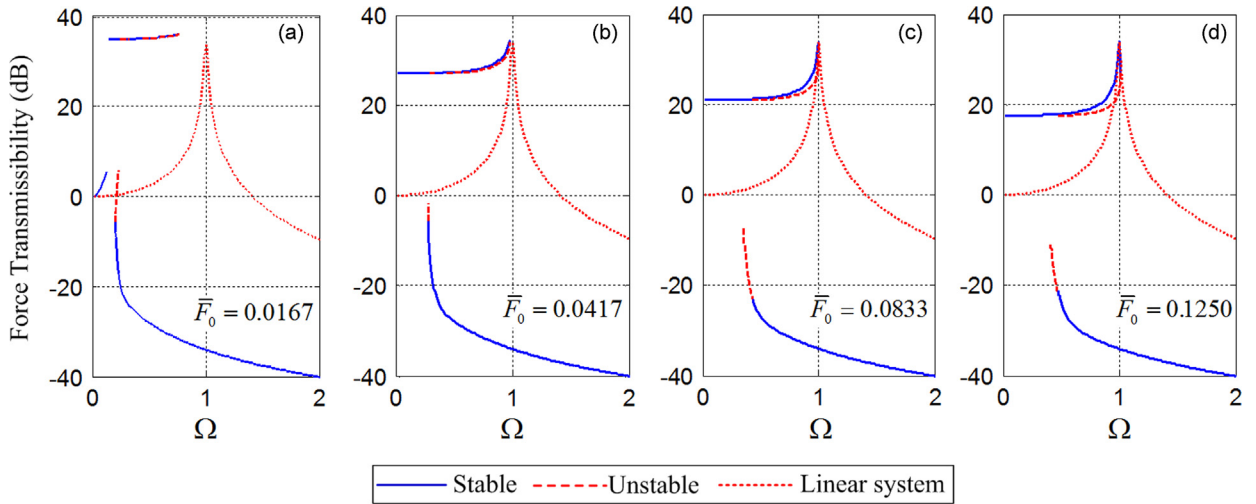


Fig. 17. Effects of excitation amplitude on force transmissibility, when $\bar{\delta}_{QZS} = 0.9$, $\eta = 0.5$, and $\zeta = 0.01$.

where $\bar{f}_t(\bar{t}_i)$ and $\bar{f}(\bar{t}_i)$ are time histories of the transmitting force and the excitation, respectively,

$$\bar{f}_t(\bar{t}_i) = \begin{cases} 2\zeta\bar{x}'(\bar{t}_i) + \left[1 - \frac{1}{\bar{\delta}_{QZS}} \left(1 + \frac{\bar{\delta}_{QZS} - 1}{\sqrt{1 - [\bar{x}(\bar{t}_i)]^2}}\right)\right] \bar{x}(\bar{t}_i) & |\bar{x}(\bar{t}_i)| < \bar{x}_d \\ 2\zeta\bar{x}'(\bar{t}_i) + \bar{x}(\bar{t}_i) & |\bar{x}(\bar{t}_i)| \geq \bar{x}_d \end{cases} \quad (39)$$

$$\bar{f}(\bar{t}_i) = \bar{F}_0 \cos(\Omega\bar{t}_i) \quad (40)$$

where $\bar{x}(\bar{t}_i)$ is the history of the displacement response obtained by solving Eq. (17) numerically.

Fig. 16 shows the analytical and numerical force transmissibility of the QZS system, respectively, compared with that of the linear system. The analytical results are obtained by using Eq. (37), and the numerical results by using Eq. (38). It is observed that there is a good agreement between analytical results and numerical ones, especially on the lower branch, excepting the ultra-low excitation frequency tending toward zero. The discontinuity of the curve of analytical results can be attributed to the fact that the expression of the force transmissibility, i.e. Eq. (37), is not continuous.

It is also can be seen from Fig. 16 that the resonance occurs at $\Omega = 1$, as the linear system, and the maximum force transmissibility of the QZS system is almost the same as that of the linear system. The jump-down frequency slightly exceeds 1 no matter how large the excitation amplitude is. Generally, the nonlinear isolator is effective when the excitation frequency is above the jump-down frequency, but it should be larger than $\sqrt{2}$ times the natural frequency for a linear isolator. Furthermore, in the effective frequency range of vibration isolation, the force transmissibility of the QZS isolator is much lower than that of the linear one. Therefore, as stated in many references [4,6,9], the QZS isolator outperforms the linear one.

The effect of excitation amplitude on the force transmissibility is illustrated in Fig. 17, showing that increasing excitation amplitude induces larger jump-down frequency, but it never excessively exceed 1. At low frequency, the upper branch of the force transmissibility curve rises up as the excitation amplitude decreases, but in the effective frequency range of vibration isolation, the force transmissibility hardly influenced by the excitation amplitude. This observation is like that of a nonlinear isolation system with the restoring force with cubic polynomial form, such as the QZS isolator in [4].

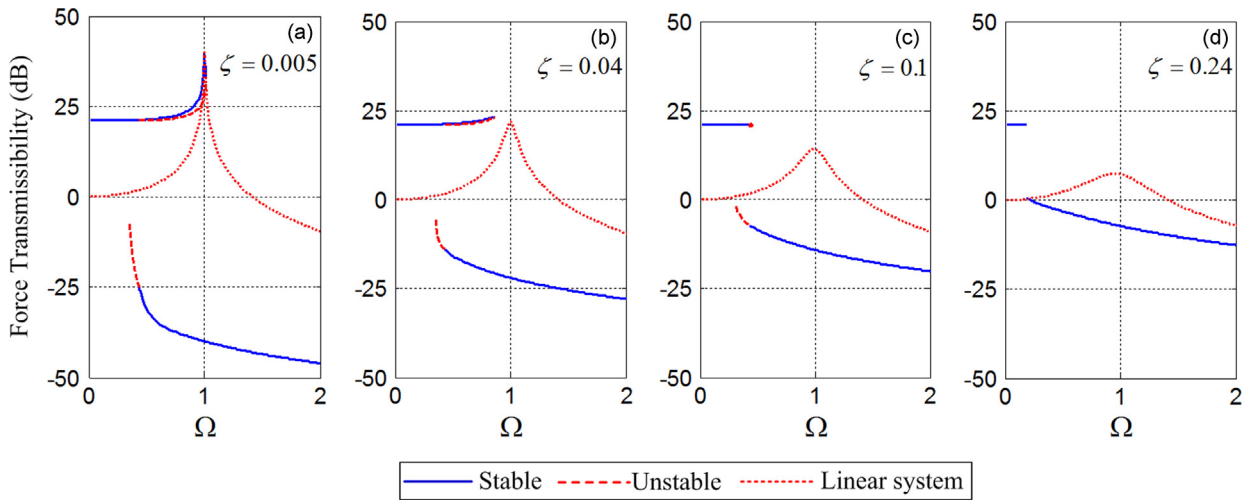


Fig. 18. Effects of damping on force transmissibility, when $\bar{\delta}_{QZS} = 0.9$, $\eta = 0.5$, $\bar{F}_0 = 0.0833$.

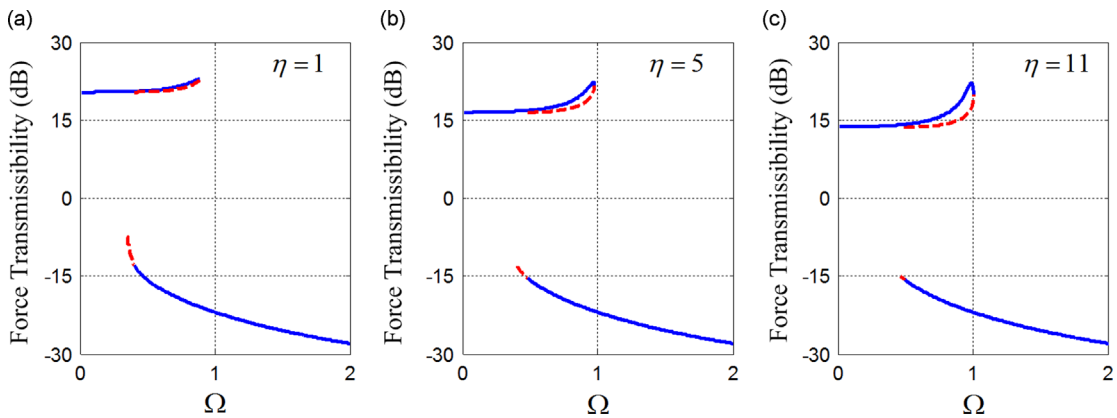


Fig. 19. Influence of η on force transmissibility, when $\bar{\delta}_{QZS} = 0.9$, $\bar{F}_0 = 0.0833$, $\zeta = 0.04$.

A particular behavior of the QZS isolator with CRSMs is that the jump-down frequency never overshoots the starting isolation frequency of the linear counterpart, and the peak transmissibility also never goes beyond that of the linear counterpart, no matter how large the excitation amplitude is, as shown in Fig. 17. However, the jump-down frequency of Carrella's QZS isolator [3,4] substantially increases as the excitation amplitude increases. In this regard, for large excitations, the present QZS isolator is superior to Carrella's one that stands for a common type of QZS isolators with different mechanisms.

Fig. 18 illustrates the impact of the damping on the force transmissibility. The jump-down frequency and transmissibility peak are all reduced as damping increases. Unfortunately, the increasing damping makes the isolation performance worse. Therefore, there is a trade-off between the effective isolation frequency and the performance, when we design a QZS isolator.

The effect of η on the force transmissibility is plotted in Fig. 19. It is observed that the jump-down frequency and the force transmissibility on the upper branch are influenced by η , but the force transmissibility in the effective frequency range of vibration isolation hardly impacted by η . However, for low-frequency vibration isolation, the small value of η is expected.

5. Experimental apparatus and results

An experimental prototype is built to test the performance of vibration isolation of the QZS system. The performance will be evaluated in terms of the force transmissibility in comparison with its linear counterpart. The experimental setup is presented in Fig. 20. An exciter is rigidly mounted on the frame (8) on the top of the QZS isolator. The amplifier (1) is used to control excitation force of the vibration exciter; the analyzer (2) supplies excitation signal to the vibration exciter and also executes data acquisition; the charge amplifier (3) magnifies the signal of four force sensors (7) symmetrically mounted in between the base and isolator in order to measure the transmitted force to the base; a force sensor (5) is installed between

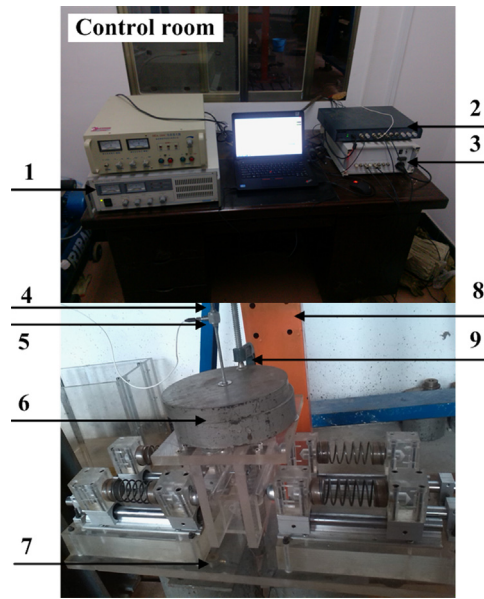


Fig. 20. Experimental setup. 1—amplifier for vibration exciter, 2—data acquisition and analyzer, 3—charge amplifier for force sensor 7, 4—connector to vibration exciter, 5—force sensors acquiring excitation force, 6—mass, 7—force sensor acquiring the transmitted force to the base, 8—frame used to fix exciter, 9—pliers used to attach the mass to the loading support.

Table 1
Parameters of the experimental prototype of the QZS system.

Parameter	Value
k_v	9.06 N/mm
k_h	4.82 N/mm
r_1	8 mm
r_2	12.5 mm
M	15 kg

Table 2
Root mean square of excitation force.

Frequency (Hz)	0.5	1	1.5	2	2.5	3	3.5	4	4.5	5	5.5–8	8.5–20
Excitation (N)	3.82	12.1	6.84	7.31	13.8	19.0	20.6	22.5	26.7	26.0	≈ 75.0	≈ 130

the exciter and mass (6) through the connector (4) to collect the excitation force; a pair of pliers (9) is used to firmly tighten the mass to the loading support.

The parameters of the experimental prototype of the QZS system are listed in Table 1. Note that the stiffness of each horizontal coil spring is 2.41 N/mm, and there are two parallel springs in the horizontal direction. Thus, the horizontal stiffness k_h in Eq. (2) is 4.82 N/mm. The vibration exciter is rigidly fixed on the support frame, and the maximum displacement of the exciter is 10 mm, while the critical displacement amplitude of contact is $x_d = \sqrt{r_2(2r_1 + r_2)} = 18.87$ mm. Therefore, in experimental tests, the disengagement between the cam and roller does not occur.

The experimental work [9] stated that the oscillation amplitude should be maintained sufficient large in experiments in order to observe the effect of negative stiffness. In this regard, for low frequency band, small excitation forces are implemented, but for high frequency band relatively large excitation forces are needed. The root mean square (RMS) of excitation forces at different frequency are listed in Table 2. Note that the force transmissibility is defined as the ratio of RMS of the transmitted force to that of the excitation force. For comparison purpose, the linear counterpart which is set by removing the cam–roller–spring mechanism from the QZS system is tested as well.

The experimental results of the force transmissibility of the QZS vibration isolation system are shown in Fig. 21, compared with those of its linear counterpart. Vibration isolation plays the role when the transmissibility is less than one. For the QZS system the frequency that vibration isolation takes effect is about 3 Hz, while for the linear system the frequency of vibration isolation is 5.53 Hz. The results indicate that the QZS system can attenuate vibration in lower frequency band. For the frequency band 3–10 Hz, the QZS system obviously outperforms in comparison with the linear one.

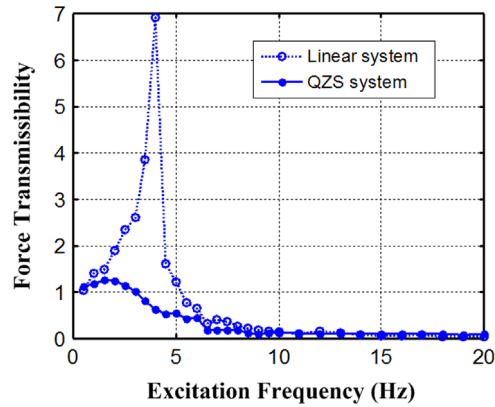


Fig. 21. Experimental results of force transmissibility of QZS system compared with linear system.

Another benefit is that the resonance of the QZS system is largely suppressed in comparison with the linear one. It is because the stiffness of the QZS system is very small so that the damping ratio for the QZS system is high, which damps down the resonance effect. At the same time, the jumping phenomenon is also suppressed by the large damping ratio. In other words, the QZS system is sensitive to damping, such as the friction in between the moving parts. However, the damping effect does not badly degenerate the isolation efficiency over the whole frequency band. As frequency increases, the performance of vibration isolation for the both systems tends to be equivalent. Overall, it can be concluded that the QZS system outperforms the linear counterpart, especially at low frequency band.

6. Conclusions

A prototype of QZS vibration isolator with cam–roller–spring mechanisms has been developed. The static and dynamic characteristics have been studied based on a piecewise nonlinear model. The compression of the horizontal spring, at the static equilibrium position, is a key parameter to control the flatness of the stiffness curve. It shows that when setting the compression smaller than but close to 1 it can achieve a large displacement range with small stiffness, which is very useful to low-frequency vibration isolation.

The equation of motion of the QZS vibration isolation system has been solved by using the averaging method. The analytical solutions are used to derive the amplitude–frequency relationship. The amplitude–frequency curve severely bends due to the strong nonlinearity. The critical condition for the disengagement between the cam and roller has been found. The jump-down frequency, namely the starting frequency of isolation for nonlinear vibration isolator, increases as the excitation amplitude increases. However, it should be noted that the starting frequency of isolation and peak transmissibility never overshoot those of the linear counterpart no matter how large the excitation is applied. The jump-down frequency is very sensitive to the variation of damping. Increasing damping shortens the resonance branch shapely, and even eliminates it, but makes the isolation performance worse. With an increase in the ratio of the roller's radius to that of the cam, the displacement range for contact between the roller and the cam decreases, and the QZS system becomes more effortless to resonate at the natural frequency of the linear system. Therefore, it is can be concluded that both a reasonable damping and a relatively small ratio of the roller's radius to that of the cam are satisfactory for the QZS isolator with CRSMs.

The prototype of the QZS isolator has been tested and the experimental results of the force transmissibility have been carried out. The results indicate that the QZS isolator outperforms the linear counterpart, especially at low frequency. Due to the limitation of the experimental apparatus and setup, the disengagement between the cam and roller did not occur in the experimental tests. The dynamic responses and force transmissibility for the cases of disengagement have been discussed in theoretical analysis.

Acknowledgment

The authors would like to appreciate Mr. Penglei Ding for his assistance for experimental tests. This research work was supported by National Natural Science Foundation of China (11102062), Specialized Research Fund for the Doctoral Program of Higher Education (20110161120040, 20130161110037), and Fundamental Research Funds for the Central Universities.

References

- [1] P. Alabuzhev, A. Gritchin, L. Kim, G. Migirenko, V. Chon, P. Stepanov, *Vibration Protecting and Measuring System with Quasi-Zero Stiffness*, Taylor & Francis Group, New York, 1989.
- [2] R.A. Ibrahim, Recent advances in nonlinear passive vibration isolators, *Journal of Sound and Vibration* 314 (3–5) (2008) 371–452.

- [3] A. Carrella, M.J. Brennan, T.P. Waters, Static analysis of a passive vibration isolator with quasi-zero-stiffness characteristic, *Journal of Sound and Vibration* 301 (3–5) (2007) 678–689.
- [4] A. Carrella, M.J. Brennan, I. Kovacic, T.P. Waters, On the force transmissibility of a vibration isolator with quasi-zero-stiffness, *Journal of Sound and Vibration* 322 (4–5) (2009) 707–717.
- [5] A. Carrella, M.J. Brennan, T.P. Waters, V. Lopes Jr, Force and displacement transmissibility of a nonlinear isolator with high-static-low-dynamic-stiffness, *International Journal of Mechanical Sciences* 55 (1) (2012) 22–29.
- [6] T.D. Le, K.K. Ahn, A vibration isolation system in low frequency excitation region using negative stiffness structure for vehicle seat, *Journal of Sound and Vibration* 330 (2011) 6311–6335.
- [7] T.D. Le, K.K. Ahn, Experimental investigation of a vibration isolation system using negative stiffness structure, *International Journal of Mechanical Sciences* 70 (2013) 99–112.
- [8] D. Xu, Y. Zhang, J. Zhou, J. Lou, On the analytical and experimental assessment of performance of a quasi-zero-stiffness isolator, *Journal of Vibration and Control* 20 (15) (2014) 2314–2325.
- [9] D. Xu, Q. Yu, J. Zhou, S.R. Bishop, Theoretical and experimental analyses of a nonlinear magnetic vibration isolator with quasi-zero-stiffness characteristic, *Journal of Sound and Vibration* 332 (14) (2013) 3377–3389.
- [10] S.E. Woodard, J.M. Housner, Nonlinear behavior of a passive zero-spring-rate suspension system, *Journal of Guidance, Control, and Dynamics* 14 (1) (1991) 84–89.
- [11] D. Platus, Negative-stiffness-mechanism vibration isolation systems, *Proceedings of the SPIE's International Symposium on Vibration control in Microelectronics, Optics and Metrology*, 1991.
- [12] A. Carrella, M. Friswell, A passive vibration isolator incorporating a composite bistable plate, *Proceedings of the Sixth EUROMECH Nonlinear Dynamics Conference (ENOC 2008)*, Saint Petersburg, Russia 2008.
- [13] A.D. Shaw, S.A. Neild, D.J. Wagg, P.M. Weaver, A. Carrella, A nonlinear spring mechanism incorporating a bistable composite plate for vibration isolation, *Journal of Sound and Vibration* 332 (24) (2013) 6265–6275.
- [14] X. Liu, X. Huang, H. Hua, On the characteristics of a quasi-zero stiffness isolator using Euler buckled beam as negative stiffness corrector, *Journal of Sound and Vibration* 332 (14) (2013) 3359–3376.
- [15] N. Zhou, K. Liu, A tunable high-static-low-dynamic stiffness vibration isolator, *Journal of Sound and Vibration* 329 (2010) 1254–1273.
- [16] X. Sun, J. Xu, X. Jing, L. Cheng, Beneficial performance of a quasi-zero-stiffness vibration isolator with time-delayed active control, *International Journal of Mechanical Sciences* 82 (2014) 32–40.
- [17] B. Tang, M.J. Brennan, On the shock performance of a nonlinear vibration isolator with high-static-low-dynamic-stiffness, *International Journal of Mechanical Sciences* 81 (2014) 207–214.
- [18] H.-J. Ahn, A unified model for quasi-zero-stiffness passive vibration isolators with symmetric nonlinearity, *Proceeding of the ASME 2010 International Design Engineering Technical Conferences & Computers and Information in Engineering Conference*, Montreal, Quebec, Canada, 2010.
- [19] A.H. Nayfeh, D.T. Mook, *Nonlinear Oscillations*, John Wiley & Sons, Inc., New York, 1995.
- [20] F.C. Moon, *Chaotic Vibrations: An Introduction for Applied Scientists and Engineers*, John Wiley & Sons, New York, 1987.
- [21] B. Ravindra, A.K. Mallik, Performance of non-linear vibration isolators under harmonic excitation, *Journal of Sound and Vibration* 170 (3) (1994) 325–337.
- [22] J.-J. Lou, S.-J. Zhu, L. He, Q.-W. He, Experimental chaos in nonlinear vibration isolation system, *Chaos, Solitons & Fractals* 40 (3) (2009) 1367–1375.